JGR Oceans

RESEARCH ARTICLE
10.1029/2018JC014437

Fission of Shoaling Internal Waves on the Northeastern Shelf of the South China Sea

Xiaolin Bai[1,2], Zhiyu Liu[1], Quanan Zheng[3], Jianyu Hu[1], Kevin G. Lamb[2], and Shuqun Cai[4]

[1]State Key Laboratory of Marine Environmental Science, and Department of Physical Oceanography, College of Ocean and Earth Sciences, Xiamen University, Xiamen, China, [2]Department of Applied Mathematics, University of Waterloo, Waterloo, Ontario, Canada, [3]Department of Atmospheric and Oceanic Science, University of Maryland, College Park, MD, USA, [4]State Key Laboratory of Tropical Oceanography, South China Sea Institute of Oceanography, Chinese Academy of Sciences, Guangzhou, China

Key Points:
- High-frequency internal waves were continuously recorded from moored observations in July 2011 in the northeastern South China Sea
- Satellite images indicate that the observed high-frequency internal wave trains were generated from fission of internal solitary waves
- The ISW fission characteristics are investigated using an analytical model, a two-layer weakly nonlinear numerical model, and a continuously stratified fully nonlinear numerical model

Correspondence to:
Z. Liu,
zyliu@xmu.edu.cn

Citation:
Bai, X., Liu, Z., Zheng, Q., Hu, J., Lamb, K. G., & Cai, S. (2019). Fission of shoaling internal waves on the northeastern shelf of the South China Sea. *Journal of Geophysical Research: Oceans*, *124*, 4529–4545. https://doi.org/10.1029/2018JC014437

Received 1 AUG 2018
Accepted 20 MAY 2019
Accepted article online 29 MAY 2019
Published online 4 JUL 2019

Abstract Using high-resolution full-water column velocity data at a site of 60-m depth on the northeastern shelf of the South China Sea, we observed high-frequency internal waves (HIWs) occurring continuously on the continental shelf during the 15-hr observation on 13-14 July 2011. This phenomenon is in contrast to the regular occurrence of internal solitary waves (ISWs) that are generally phase-locked to the tides. We hypothesize that the continuously occurring HIWs are generated from shoaling ISWs via fission. Analysis of the Moderate Resolution Imaging Spectroradiometer (MODIS) true-color images supports this hypothesis. The mechanism of ISW fission is then investigated using an analytical model as well as a two-layer weakly nonlinear numerical model based on the regularized long-wave (RLW) equation. The results are also compared with those from a fully nonlinear continuously stratified numerical model. Simulation results are generally consistent with the field measurements, explaining the observations of the continuous occurrence of HIWs. Sensitivity experiments are conducted to investigate the role and effects of the initial wave amplitude, pycnocline depth and thickness, bathymetry, and viscosity on ISW fission. Although all these factors impact the properties of the shoaling ISWs, both the two-layer and continuously stratified models suggest that fission mainly occurs near the critical point region, highlighting the importance of pycnocline depth. However, simulations using the two-layer model suggest that fission occurs after ISWs pass through critical points, whereas the fission location predicted by the continuously stratified model is generally offshore of critical points. This points to the deficiency of the two-layer model in simulating small-amplitude short trailing waves, large-amplitude ISWs, wave breaking, and higher-mode waves.

1. Introduction

Nonlinear internal waves, often in the form of internal solitary waves (ISWs), are an omnipresent phenomenon in stratified oceans, fjords, and lakes all around the world. These waves have received much attention over the last a few decades due to their long-range propagation, large amplitudes estimated up to 170 m in the South China Sea (SCS; Klymak et al., 2006), regular occurrence (e.g., type-a and type-b ISWs in the northern SCS first identified by Ramp et al., 2004), vital role in oceanic energy cascade, and substantial contributions to ocean mixing (Lamb, 2014).

As one of the predominant regions with energetic ISWs, the SCS has been of great interest to the international oceanographic community for several decades. A series of studies have been carried out to look into the properties and dynamics of the ISWs based on field observations (e.g., Alford et al., 2010; Apel et al., 1997; Klymak et al., 2011; Ramp et al., 2004), satellite imagery (e.g., Zhao et al., 2003, 2004; Zheng et al., 2007) and numerical simulations (e.g., Buijsman et al., 2012; Vlasenko et al., 2010). Taken together, these studies have reached a consensus that the ISWs usually evolve from large baroclinic tides under the combined effects of nonlinear steepening and dispersion, with the baroclinic tides being mainly generated by the interaction of strong barotropic tides with large ridges in the Luzon Strait. During their propagation onto the continental slope and shelf, the ISWs deform, change polarity, fission, and eventually dissipate (Lamb, 2014). Numerous studies on shoaling ISWs have been carried out in the northern SCS. From synthetic aperture radar images, Liu et al. (1998) identified wave steepening and polarity conversion from depression to elevation ISWs, which were then documented by Orr and Mignerey (2003) in field

observations. Fu et al. (2012) observed shoaling of large amplitude ISWs from intensive moored measurements. Lien et al. (2012) observed shoaling ISWs with trapped cores over the continental slope. Overall, these efforts have substantially advanced our understanding of the generation and propagation of ISWs.

Less attention has been paid to the dynamics of ISW fission or the properties of the fissioned internal waves. It is clear from satellite observations that a single ISW usually fissions into a wave train consisting of a number of higher-frequency waves (e.g., Jackson et al., 2011; Liu et al., 1998). Field measurements of acoustic backscatter have also revealed prototypical structures of the generated higher-frequency waves, such as those of Orr and Mignerey (2003) in the SCS and of Shroyer et al. (2009) off the New Jersey Coast. Moreover, numerical simulations (e.g., Cai et al., 2002; Grimshaw et al., 2010; Liu et al., 1998; Small, 2001; Tappert & Zabusky, 1971; Zheng et al., 2001) have also been carried out to study the fission process. For example, Small (2001) and Cai et al. (2002) studied fission of ISWs using weakly nonlinear models. Grimshaw et al. (2014) analyzed the combined effects of rotation and topography on the fission process. Analytical solutions of ISW fission in a horizontally varying pycnocline were obtained by Tappert and Zabusky (1971). These were then applied to the study of ISWs in the Gulf of Aden by Zheng et al. (2001). However, these studies were mostly targeted at verifications of fission occurrence or estimations of the number of internal waves in the generated wave train, leaving the dynamical characteristics of the generated wave train and the role of ISW fission in wave dissipation unexplored.

Our recent observations (Bai et al., 2013) revealed an abundance of high-frequency internal waves (HIWs) on the northeastern shelf of the SCS, a region sometimes referred to as the southern Taiwan Strait as indicated by a black box in Figure 1a. Examples of the ISW imprints at the sea surface along two transects indicated in Figure 1a are shown in Figures 1b and 1c. The plotted values were extracted from a Moderate Resolution Imaging Spectroradiometer (MODIS) true-color image on 30 June 2003 along two transects indicated by the green and red lines in Figure 1a. In the northern part of the study region, a wave train consisting of at least five waves was present. By contrast, there was only a single wave in the southern part. Given that the waves in the two parts originated from a same ISW front that propagated from the Luzon Strait (Bai et al., 2014), a question naturally arises as to why the ISW front had evolved differently on the continental shelf.

Based on solutions of the Perturbed Korteweg-de Vries equation, Bai et al. (2013) argued that the HIWs observed in the northern part were generated because of the shoaling topography. However, our knowledge on the dynamical evolution of shoaling ISWs remains limited. Here we propose and test the hypothesis that fission of ISWs is responsible for the generation of the observed HIWs. We will first describe properties of the generated HIWs based on both in situ and satellite remote sensing observations. We then conduct a dynamical analysis to elaborate the mechanism of ISW fission.

The rest of the paper is organized as follows. In section 2, we describe in situ observations of HIW trains. In section 3, we show satellite evidence of ISW fission. We then conduct a dynamical analysis of ISW fission based on an analytical model in section 4, and a two-layer weakly nonlinear numerical model in section 5 . These results are compared with numerical simulations of a fully nonlinear model using continuous stratification in section 6. We summarize our main results in section 7.

2. Field Measurements

Field measurements were conducted onboard the R/V *Yanping II* on the northeastern shelf of the SCS in July 2011. During the cruise survey, profiling measurements of temperature and conductivity were made with a SeaBird SBE 25 conductivity-temperature-depth (CTD) profiler. A bottom-mounted 600-kHz acoustic Doppler current profiler (ADCP) was deployed at 60 m depth (118.167°E, 22.381°N, Station B in Figure 1a) to measure both the horizontal and vertical velocities throughout the water column. The bin size of the ADCP was set to 2 m, and it was configured to sample with a time interval of 4 s. Reliable velocity measurements were obtained from 18:00 (UTC+8) on 13 July to 09:00 (UTC+8) on 14 July. All these data were processed after a series of quality control steps.

To reveal properties of internal waves, we focus on analysis of the vertical velocity and baroclinic horizontal velocities. The baroclinic current $\vec{U}_{bc}(z,t)$ is derived from the observed horizontal current $\vec{U}(z,t)$, i.e., $\vec{U}_{bc}(z,t) = \vec{U}(z,t) - \vec{U}_{bt}(t)$, where the barotropic current $\vec{U}_{bt}(t)$ is simply defined as the depth-mean current,

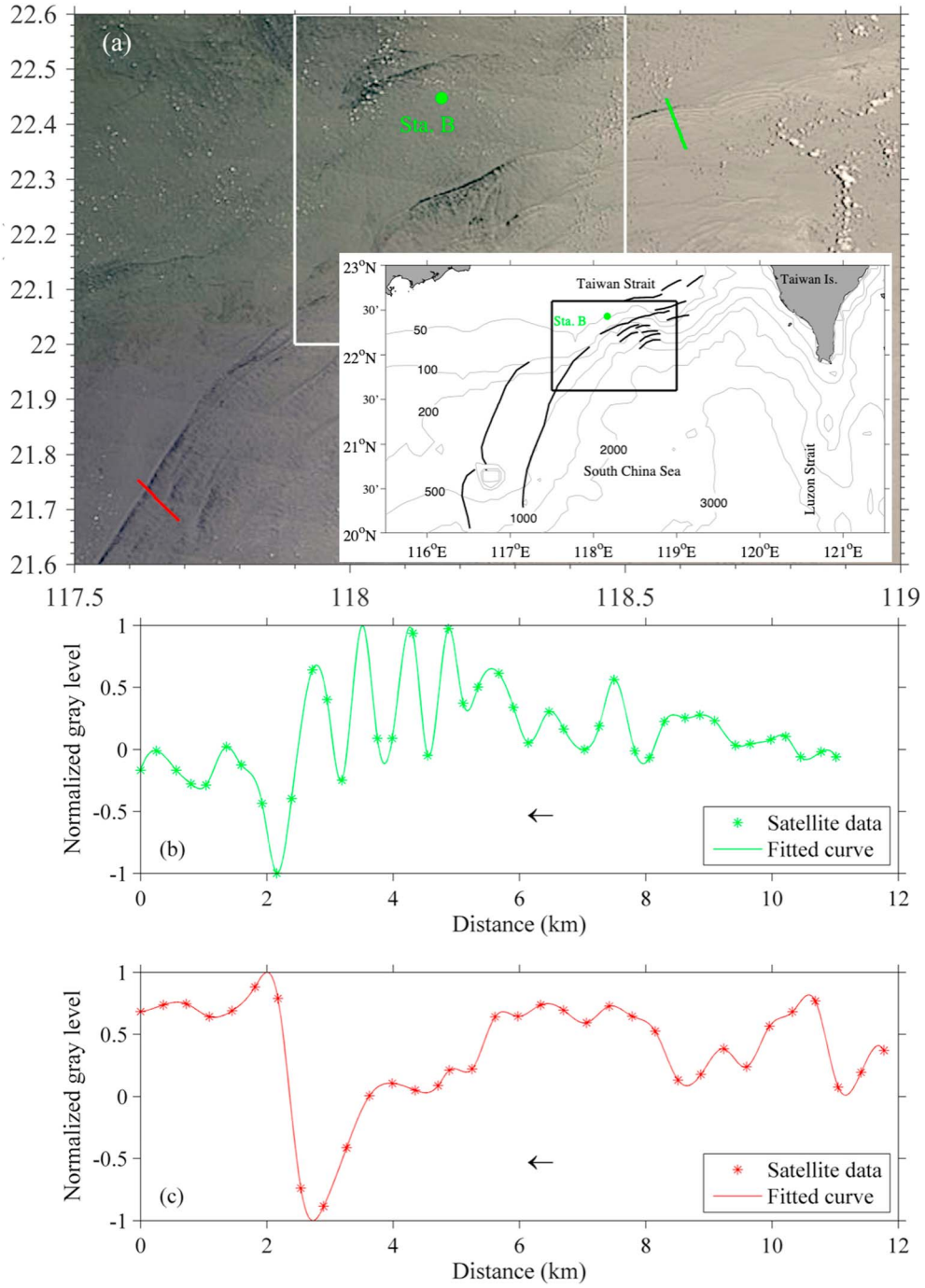

Figure 1. (a) Sub-scene of a Moderate Resolution Imaging Spectroradiometer (MODIS) true-color image taken on 30 June 2003 at 02:55 (UTC). The region of this image is denoted by a black box in the inserted map, with the internal solitary waves (ISWs) visible in MODIS image shown as black thick lines. The white box overlain the image is a region near Station B and zoomed in Figure 3a. Isobaths are labeled in meters, obtained from ETOPO1 database. The variations of gray scale along the green and red lines are shown in (b) and (c), respectively. Arrows point out the direction of internal solitary wave propagation (i.e., shoreward). Star points are from MODIS data, which are connected by fitted splines.

that is, $\overrightarrow{U}_{bt}(t) = \frac{1}{H}\int_{-H}^{0}\overrightarrow{U}(z,t)dz$. These velocity vectors all have two components: the zonal velocity u and the meridional velocity v, that is, $\overrightarrow{U} = (u, v)$, $\overrightarrow{U}_{bt} = (u_{bt}, v_{bt})$, and $\overrightarrow{U}_{bc} = (u_{bc}, v_{bc})$. The temporal variations of u_{bt} and v_{bt} suggest that the barotropic flow was predominantly due to semidiurnal tides (Figure 2a).

Figure 2b shows time-depth variations of the vertical velocity. Strikingly, upward and downward velocities appeared alternately throughout the whole water column, suggesting the influence of mode-1 internal waves. More interestingly, although varied in intensity, internal waves appeared to be present throughout the entire 15-hr observation period. This is in contrast to previous observations that ISWs usually appear as discrete wave packets phase-locked to the tides. To visualize the detailed structures of these waves, we select two observation periods as shown in Figures 2c1 and 2c3 (for Event 1, 02:30 to 05:00 [UTC+8] on 14 July 2011) and Figures 2d1-2d3 (for Event 2, 05:30 to 08:00 [UTC+8] on 14 July 2011), respectively. To see the influence of internal waves more clearly, we also project the baroclinic flow to the cross-isobath direction (positive shoreward) and along-isobath direction (positive 90° clockwise of the shoreward direction). For Event 1, there were 22 waves during the 2.5-hr period, as indicated by 22 pairs of upward and downward velocities in Figure 2c3. As such, the average period of the internal waves is estimated to be 6.8 min, which is similar to the observations of Bai et al. (2013) at a nearby location (118.828°E, 22.576°N, their Station A8). Positive values of the cross-isobath baroclinic velocity u_{bc} in the lower layer suggest that this group of HIWs consists of waves of elevation (Figure 2c1). For Event 2, there were eight waves with relatively small amplitudes between 05:30 and 06:00. The maximum horizontal velocity layer deepened suddenly around 06:00 from 42 to 30 m above the seabed. Afterwards, following an ISW of elevation (from 06:03 to 06:20), a group of large-amplitude (~15 m) HIWs consisting of at least seven waves appeared between 06:30 and 07:00 on 14 July 2011. The average period of these waves was 4.3 min, shorter than that in Event 1.

To conclude, field measurements in the southern Taiwan Strait suggest the persistent presence of HIWs over the steep slope, which is consistent with satellite observations shown in Figure 1. We hypothesize that fission of ISWs is responsible for the generation of the observed HIWs. In the following sections, we test this hypothesis with both satellite observations and dynamical analysis.

3. Satellite Observations

The observed HIWs on the northeastern shelf of the SCS are visible in satellite images. The spatial distribution and temporal variations of the HIWs have been presented and discussed by Bai et al. (2014) based on analysis of the MODIS true-color images. Here using additional satellite images, we intend to show that the ISWs are indeed subject to fission as they propagate onto the continental slope and shelf over the shoaling topography, through which they evolve into trains of HIWs.

The MODIS true-color images are produced from calibrated, corrected, and geo-located radiance (Level-1 B) data, with a spatial resolution of 250 m (Bai et al., 2014). Two examples are shown in Figure 3. The boxed part of Figure 1a is shown in Figure 3a, while Figure 3b shows another image for the same region taken at 05:15 (UTC) on 24 June. To visualize the effect of topography on the evolution of ISWs, the isobaths determined from the ETOPO1 database are overlaid onto the MODIS true-color images. The ETOPO1 database has a spatial resolution of 1 arc-min (about 1.85 km). In Figure 3a, MODIS image shows the signatures of two wave packets (hereafter called Wave Packet 1 and Wave Packet 2). The leading wave packet (Wave Packet 1) is located over an underwater bump. Both the wave packets consist of a single wavefront according to their sea surface signature. In Figure 3b, there are also two wave packets. In contrast to those in Figure 3a, the two internal wave packets are closer to Station B, consisting of more than three waves in each wave packet.

The white dashed lines in Figure 3, referred to as Topo 1 and Topo 2, respectively, indicate two propagation paths of the ISWs in this region. Since the two images were both taken in June, for the purpose of qualitative analysis we can assume that the background stratifications in the region were roughly the same, and therefore, the two images can be taken together to indicate evolution features of the ISWs. A comparison of Figures 3a and 3b indicates that after crossing the bump an ISW evolves into a wave train consisting of several smaller-scale waves. This is even clearer in Figure 4, where detailed structures of both the parent ISW and the generated HIWs are shown with normalized gray scales. The black line in Figure 4a indicates the Topo 2 line in Figure 3. Here t_1 shows the region near the location of the ISW in Figure 3a, while t_2 indicates

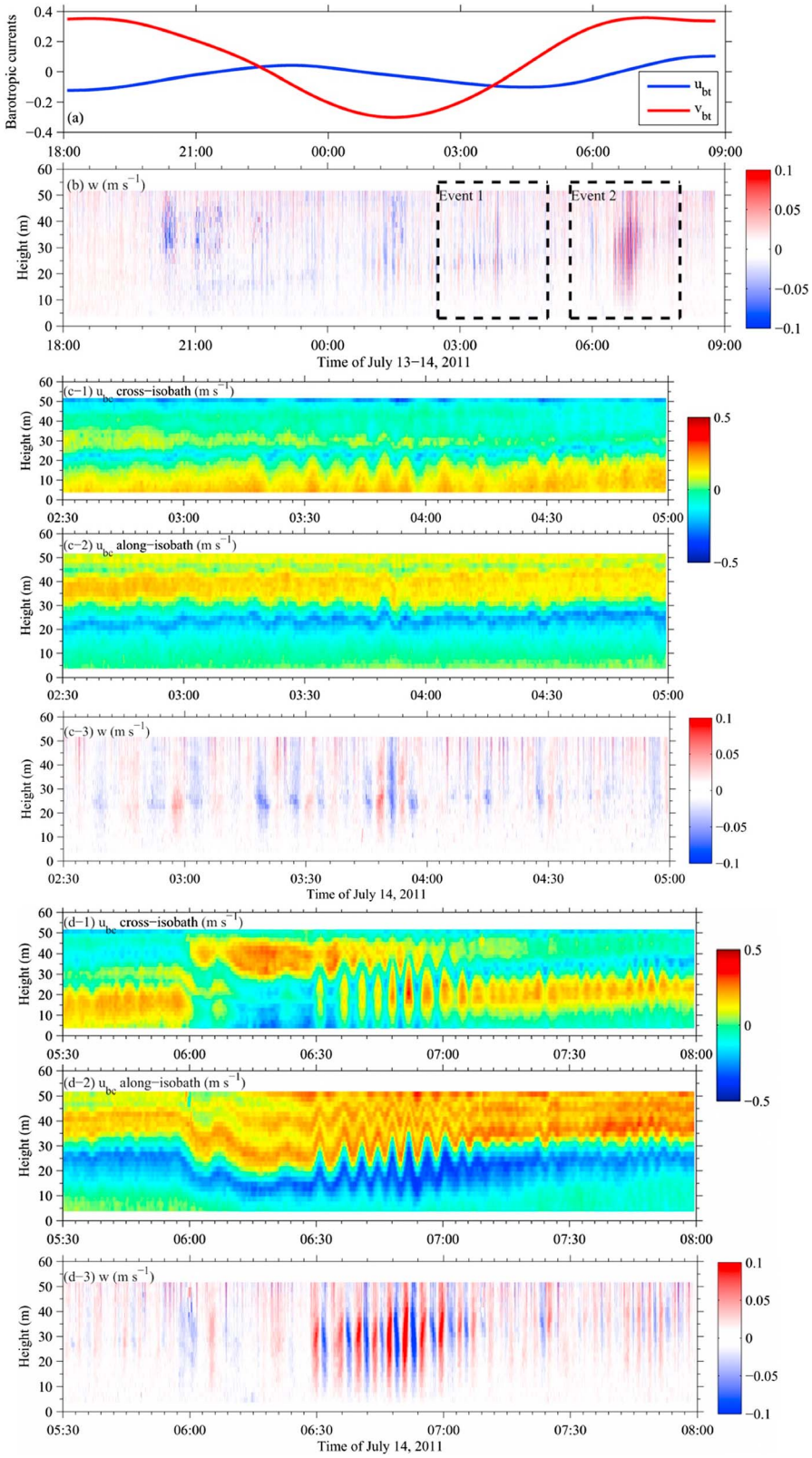

Figure 2. (a) Barotropic tidal currents [m/s] and (b) vertical velocity [m/s] observed at Station B. Two events of internal solitary wave train are indicated by dashed boxes and zoomed in lower panels: Event 1 from (c-1) to (c-3), and Event 2 from (d-1) to (d-3). The three panels represent the cross-isobath and along-isobath baroclinic velocities as well as the vertical velocity, respectively.Figure 2 (Continued). Same as (c-1) to (c-3) but for the results in Event 2.

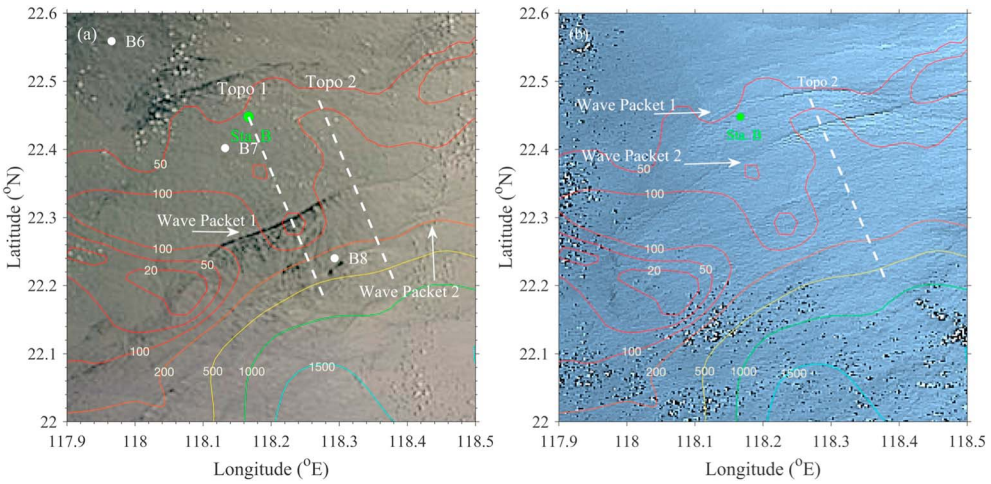

Figure 3. Zoomed-in Moderate Resolution Imaging Spectroradiometer (MODIS) true-color image in the white box region of Figure 1a: (a) at 02:55 (UTC) on 30 June 2003 and (b) at 05:15 (UTC) on 24 June 2007. The lines termed as "Topo 1" and "Topo 2" indicate the paths of the two groups of ISWs. Isobaths (20, 50, 100, 200, 500, 1,000, and 1,500) are labeled in meters, obtained from ETOPO1 database.

the region near the location of the second ISW train in Figure 3b. The corresponding wave structures along t_1 and t_2 are shown with the normalized gray level in Figures 4b and 4c. One can see that a single ISW (Figure 4b) has developed into a group of four waves (Figure 4c) after shoaling 10 km. This suggests that fission of ISWs does occur as they propagate onto the shelf over the shoaling topography, before reaching Station B.

4. Theoretical Prediction

We apply an analytical model (Tappert & Zabusky, 1971; Zheng et al., 2001) to test the hypothesis of ISW fission. As shown in Figure 5, the model includes a continental slope with a length scale L, the so-called gradient region, connecting a deep region (Region 1 with an upper layer of thickness h_{11} and density ρ_{11} and a

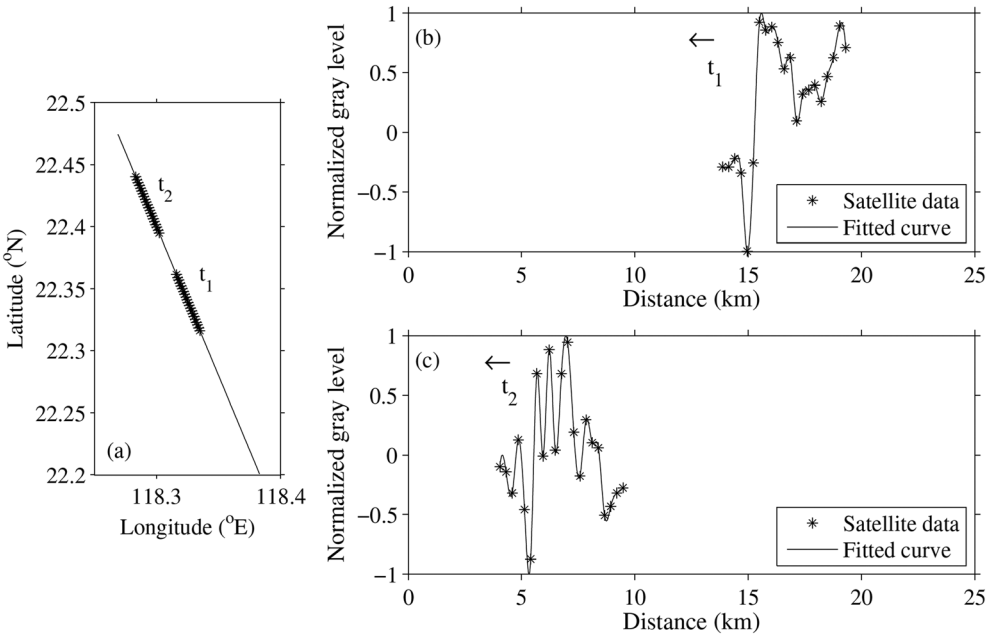

Figure 4. (a) The "Topo 2" line shown in Figure 3. Parts t_1 and t_2 denote locations of internal solitary waves in Figures 3a and 3b, respectively. Correspondingly, (b) and (c) show the variation of gray scale along parts t_1 and t_2, respectively.

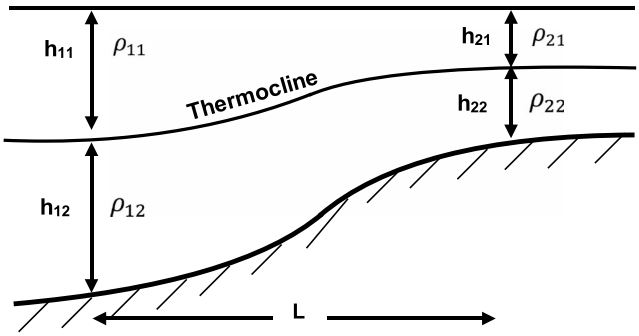

Figure 5. Schematic of a two-layer analytical model with the thermocline shoaling on the continental shelf, reproduced from Zheng et al. (2001). Parameters for the model are labeled on the panel. L is the width of the continental shelf, ρ_{i1} and h_{i1} the density and thickness of the upper layer, while ρ_{i2} and h_{i2} the density and thickness of the lower layer.

lower layer of thickness h_{12} and density ρ_{12}) and a shallow region (Region 2 with an upper layer of thickness h_{21} and density ρ_{21} and a lower layer of thickness h_{22} and density ρ_{22}). In general, an ISW may fission into numerous rank-ordered waves as it propagates from the deep region to the shallow region. Here a parameter R

$$R = \left(\frac{v_{s2}}{v_{s1}}\right)^{\frac{3}{2}} \frac{a_{s1}}{a_{s2}} \left(\frac{l_{s1}}{l_{s2}}\right)^2, \tag{1}$$

is used to predict the state of the ISWs (Tappert & Zabusky, 1971; Zheng et al., 2001). Here $v_{si}\left(=\sqrt{\frac{\delta\rho_i}{\rho_i} g \frac{h_{i1}h_{i2}}{H_i}}\right)$ is a velocity scale (with $H_i = h_{i1}+h_{i2}$), and a_{si} and l_{si} are the scales of the wave amplitude and dispersion length, respectively. ρ_i and $\delta\rho_i$ are the average density and the density difference between upper and lower layers, respectively. The subscript i indicates Region i ($i = 1$ or 2). Following the scale analysis of Zheng et al. (2001), l_{si} was chosen as the upper layer thickness so that $l_{s1} = h_{11}$ and $l_{s2} = h_{21}$ in equation (1). The wave amplitude a_{si} was assumed to have the same scale as the upper layer thickness. In this way, equation (1) can be simplified to

$$R = \left(\frac{\delta\rho_2/\rho_2}{\delta\rho_1/\rho_1} \cdot \frac{h_{22}\cdot H_1}{h_{12}\cdot H_2}\right)^{\frac{3}{4}} \left(\frac{h_{11}}{h_{21}}\right)^{\frac{9}{4}}, \tag{2}$$

If $R \le 1$, an ISW will retain its waveform; otherwise, the ISW will fission into two or more waves. The final number of waves is determined by the greatest integer N satisfying the inequality (Tappert & Zabusky, 1971; Zheng et al., 2001)

$$N \le p(R) = \left(1 + \sqrt{1 + 8R}\right)/2, \tag{3}$$

According to the observations shown in Figure 2d, the amplitude of the ISWs is approximately 15 m. Therefore, the amplitude of the wave (a) has a scale of 10 m, that is, $a = O(10\text{ m})$. Figure 6 shows the locations of three sites B8, B7, and B in relation to the two topographies shown in Figure 3a. The temperature profiles at Stations B8 and B7 are used to construct the thermocline structure along the topography. According to the temperature profiles shown in Figure 6, Station B8 should be taken as the deep region with a depth $H_1 = 155$ m, the upper layer $h_{11} = 70$ m, and $\delta\rho_1/\rho_1 = 0.0025$, while Station B7 is the shallow region with a depth $H_2 = 70$ m, the upper layer $h_{21} = 30$ m, and $\delta\rho_2/\rho_2 = 0.0033$. It can be shown that these parameters satisfy the necessary conditions given in Zheng et al. (2001; their equation (1)a to equation (1)c). As such, R is estimated to be 8.54, giving $N = 4$, suggesting that a single ISW will fission into at least 4 waves as it shoals onto the shelf. Moreover, according to the MODIS observations, the length scale l of the wave prior to fission was about 1 km (Figure 1c). Therefore, the length of the gradient region L must satisfy $l \ll L \ll (l/l_s)^2 l = O\left(l\frac{a_s}{a}\right)$, that is, 1 km $\ll L \ll O(5$ km). Given that the distance between Stations B8 and B7 is 22 km and longer than the theoretical maximum L, an ISW may be able to fission into many more waves as it propagates from Station B8 to Station B7. This suggests that the observed HIWs were very likely due to the fission of shoaling ISWs.

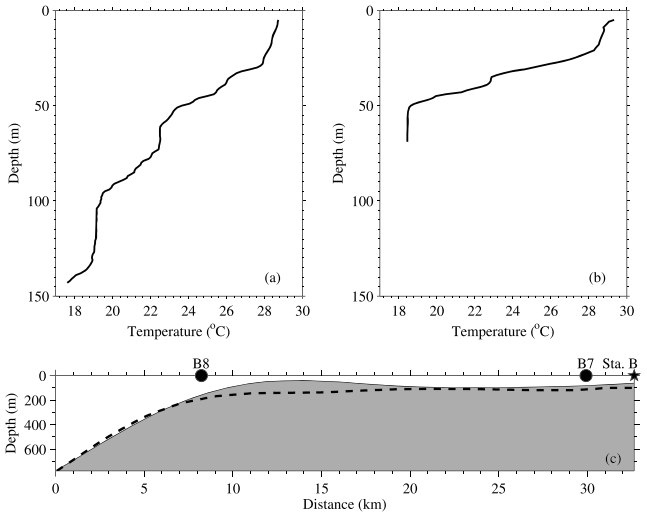

Figure 6. Observed temperature profiles at sites (a) B8 and (b) B7 on 3 July 2011 as shown in Figure 3a. (c) Locations of three sites B8, B7, and B in relation to the topography used in numerical simulations, that is, "Topo 1" (solid line in gray region) and "Topo 2" (dashed line) as shown in Figure 3.

5. Dynamical Analysis Based on a Weakly Nonlinear Model

In order to understand the generation process of the HIWs, we investigate the dynamics of ISW fission with a two-layer model based on the regularized long-wave (RLW) equation (e.g., Cai et al., 2002). We choose the RLW equation instead of the more commonly used Extended KdV (EKdV) equation (Liu et al., 1998; Orr & Mignerey, 2003; Small, 2001) for its

Table 1
Experimental Parameters for the Numerical Simulations With the RLW Equation

Case #	h_1 (m)	η_0 (m)	ε	γ_0
E2-1	70	-20	1	-10^{-5}
E2-2	70	-20	1	0
E2-3*	70	-20	0	0
E2-4	70	-30	0	0
E2-5	70	-10	0	0
E2-6	30	-20	0	0
E2-7	50	-20	0	0
E1	30	-15	0	0

Note. The asterisk represents the reference experiment. The value of η_0 is upward positive. Here the negative value represents an initial wave with the depression waveform.

stability and physically realistic property in high wavenumber components (Lamb & Xiao, 2014). For the purpose of identifying the fundamental cause of ISW fission, we consider the shoaling of ISWs in a situation without any background currents. The equation employed here is in the form (Cai et al., 2002)

$$\eta_t + c_0\eta_x + \alpha\eta\eta_x + k\eta^2\eta_x - \frac{\beta}{c_0}\eta_{xxt} - \frac{1}{2}\varepsilon\eta_{xx} + \gamma\eta = 0 \tag{4}$$

The initial ISW has the form $\eta(x,t) = -\eta_0\,\mathrm{sech}^2\left(\frac{x-Vt}{L}\right)$, with η being the interface displacement and η_0 its initial amplitude. In a two-layer system, let h_1 and h_2 be the thicknesses of the upper and lower layers of the water column, respectively, with the corresponding densities being ρ_1 and ρ_2, and let g be the gravitational acceleration. Other parameters are as follows (Cai et al., 2002): linear phase speed of the ISW $c_0 = \sqrt{\frac{g(\rho_2-\rho_1)h_1h_2}{\rho_2h_1+\rho_1h_2}}$, nonlinear phase speed of the ISW $V = c_0+\alpha\eta_0/3$, length of the ISW $L = \sqrt{12\beta/\alpha\eta_0}$, quadratic nonlinear coefficient $\alpha = \frac{3c}{2h_1h_2}\left(\frac{\rho_2{h_1}^2-\rho_1{h_2}^2}{\rho_2h_1+\rho_1h_2}\right)$, cubic nonlinear coefficient $\kappa = -\frac{3c_0\left[\left(\rho_2{h_1}^2-\rho_1{h_2}^2\right)^2+8\rho_1\rho_2h_1h_2(h_1+h_2)^2\right]}{16{h_1}^2{h_2}^2(\rho_2h_1+\rho_1h_2)^2}$, and dispersive coefficient $\beta = \frac{ch_1h_2}{6}\left(\frac{\rho_1h_1+\rho_2h_2}{\rho_2h_1+\rho_1h_2}\right)$. We solve equation (4) using the same numerical method as Cai et al. (2002). Similarly, the dissipation coefficient, ε, is set to be 0 or 1 m^2/s. The shoaling term is $\gamma = \gamma_0 D_x/|D_x|_{\max}$, where D_x is the gradient of the topography and γ_0 is set to be 0 or -10^{-5} s^{-1} (Cai et al., 2002).

In this model, we use a two-time-level and three-point Crank-Nicholson scheme to differentiate equation (4) (Cai et al., 2002). The resulting system was proven to be unconditionally stable and is second order in both time and space. Additionally, the Orlanski radiation condition is used at both ends of the computational boundaries (Orlanski, 1976). The spatial and temporal steps are $\triangle x = 30$ m and $\triangle t = 20$ s, respectively. The temporal step meets the requirement that $\triangle t < \triangle x/c_0$. Sensitivity experiments were performed to test the suitability of horizontal resolution. We compared the results using $\triangle x = 60$, 30, and 15 m. We choose $\triangle x = 30$ m in the later experiments because in the test it shows similar results with the experiment using $\triangle x = 15$ m. Realistic bottom topographies along two propagation paths of ISWs, that is, Topo 1 and Topo 2, are derived from the ETOPO1 database (Figure 6c). Compared to Topo 2, Topo 1 features an underwater bump on top of the gradually shoaling topography from the deep water to the shelf. To study general features of ISW fission, we use Topo 2 as the reference topography. In the experiments, we will compare the results using Topo 1 with that using Topo 2. Table 1 gives the detailed configurations of the experiments. Here E2 indicates the experiments using Topo 2, while E1 is the experiment using Topo 1. The dependences of ISW evolution on the parameters in equation (4), that is, stratification (h_1 versus h_2), initial amplitude (η_0), dissipation coefficient (ε) and the effect of shoaling term (γ), are studied with a set of numerical experiments. The effect of the Earth rotation is not considered here as the propagation distance of the studied ISWs is relatively short; it takes less than 10 hr for the ISWs to propagate from the deep water (800-m depth) to the shelf (100-m depth).

Results of the eight experiments are shown in Figure 7. There are two panels for each experiment: the lower panel shows the initial isopycnal interface (dashed line) over the topography (black shading) with the critical regions indicated by gray blocks, while the upper panel shows the displacement of isopycnal at different times, revealing the evolution of a shoaling ISW. The critical region is defined as the region where $|\alpha| \le 0.01$ s^{-1}, that is, where the coefficient of nonlinear term is close to zero and the ISW is changing its polarity. In each experiment, an idealized ISW initially located in the deep water ($x = 0$ km) is set to propagate toward the shelf.

5.1. Sensitivity Experiments

To reveal the generation mechanism of the HIWs, we apply the model to the reference topography (Topo 2). In experiment E2-1, both the dissipation and the shoaling terms in equation (4) are considered. The thickness of the upper layer is set as $h_1 = 70$ m according to the maximum temperature gradient in Figure 6a. The initial wave amplitude (positive upward) is set as $\eta_0 = -20$ m based on our observations,

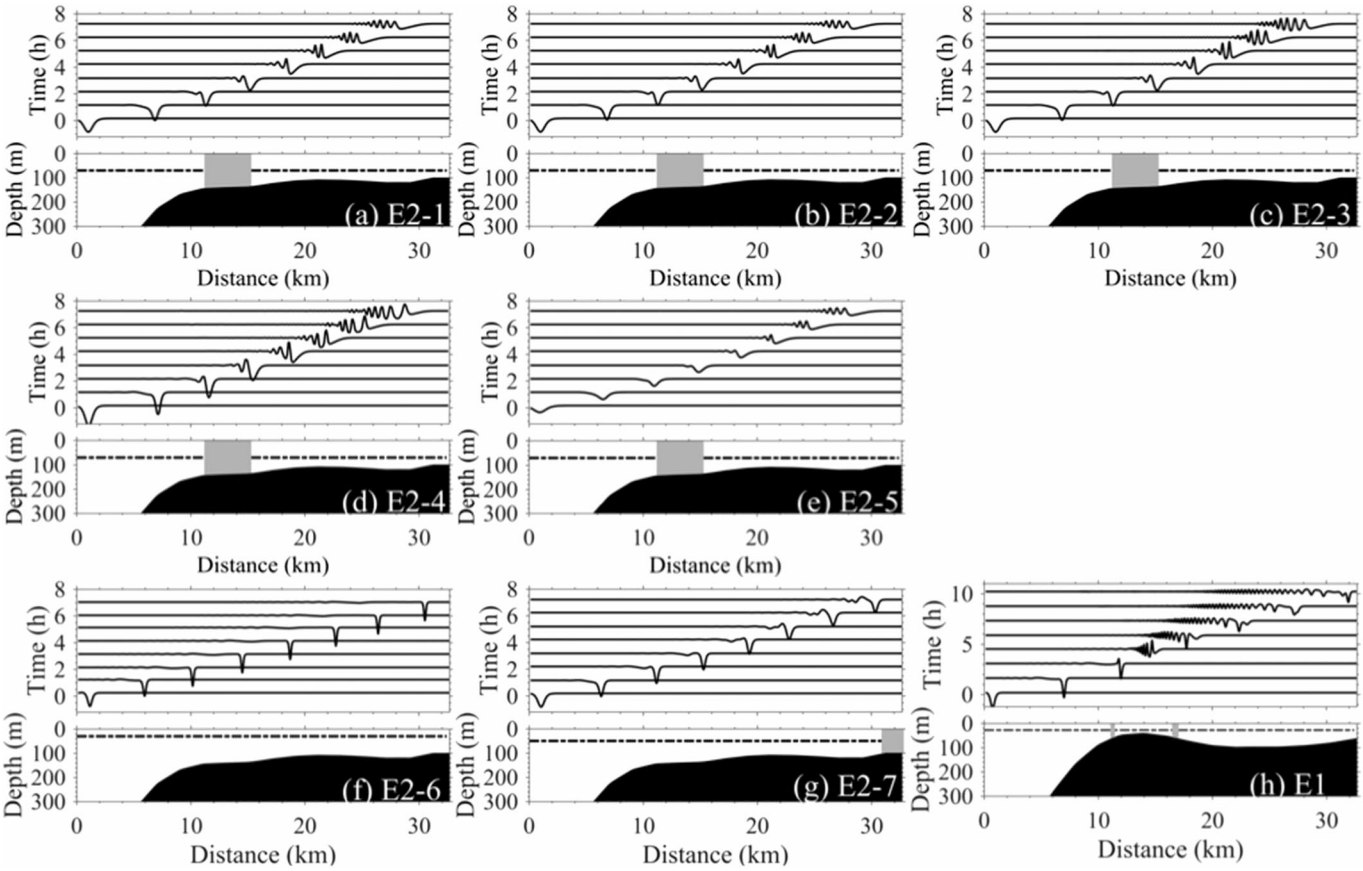

Figure 7. Evolution of a typical shoaling ISW simulated for (a to g) experiments E2-1 to E2-7 and (h) experiment E1. The critical regions (defined as$|\alpha| \leq 0.01\ \mathrm{s}^{-1}$) are indicated by gray blocks over the topography, and the horizontal dashed line indicates the depth of the density interface.

representing an ISW of depression. As shown in Figure 7a, the fission process of a shoaling ISW has been successfully simulated in this experiment. During the first 2 hr, the ISW preserves its form as it remains offshore of the critical region. By $t = 3$ hr as the ISW reaches the critical region, the rear of the wave gets steeper and the isopycnal behind the leading depression is raised above its equilibrium depth. As the wave continues shoaling and passes through the critical region at $x = 15$ km, the front of the ISW is substantially flattened. The steep rear of the wave develops into a wave of elevation and fissions into 4 waves on reaching $x = 30$ km. The waves are rank-ordered behind a largest-amplitude leading wave (e.g., Lamb & Xiao, 2014).

We have shown that the fission of an ISW can be successfully simulated but the essential dynamical cause of the process remains to be revealed. To this end, we first examine the effect of the shoaling term in experiment E2-2 by omitting the shoaling term in equation (4). As shown in Figure 7b, there is no observable difference between results of E2-1 and E2-2. It is thus suggested that the effect of shoaling term in equation (4) is not essential to the evolution of ISWs. We then similarly examine the role of dissipation. That is, we omit both the dissipation term and the shoaling term in the experiment E2-3. As shown in Figure 7c, the ISW preserves its waveform as it shoals over the slope, and starts to deform on reaching the critical region, as in E2-1 and E2-2. The ISW then fissions into a group of HIWs as it passes the critical region, at the same location as in E2-1 and E2-2. However, the amplitudes of the generated HIWs are substantially larger than in E2-1 and E2-2. This is understandable as substantial energy should have been lost in the evolution process for E2-1 and E2-2 due to the dissipation and shoaling term. Qualitatively, there is no essential difference in the fission process. The number of generated HIWs is the same in all the three experiments. We can then conclude that neither dissipation nor the effect of shoaling term is essential for the fission of ISWs. Therefore, we can look

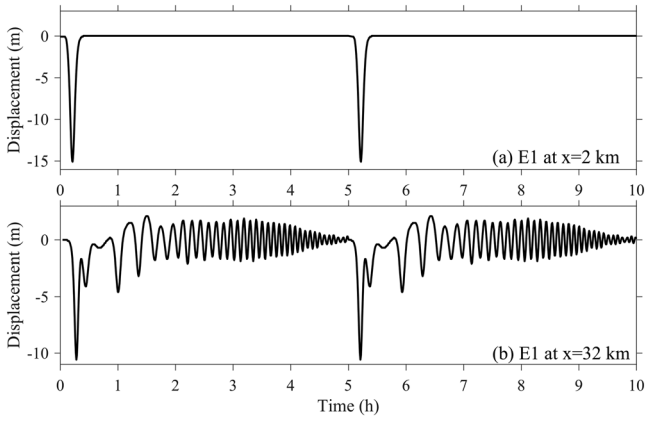

Figure 8. Time series of the interface displacement at (a) $x = 2$ km and at (b) $x = 32$ km as a result of the propagation and evolution of two initial internal solitary waves separated by 5 hr. The time interval between the two wave packets is estimated from their distance in Figure 3b.

into the dominating factor(s) of ISW fission by conducting a series of sensitivity experiments omitting the last two terms in equation (4). For this purpose, the experiment E2-3 serves as the reference case.

We first examine the impact of initial wave amplitude on the fission process. This is realized by comparing results of E2-3 (with $\eta_0 = -20$ m), E2-4 ($\eta_0 = -30$ m), and E2-5 ($\eta_0 = -10$ m). Note that to make the use of RLW equation valid, we have chosen initial wave amplitudes below the theoretical upper limit of wave amplitude for weakly nonlinear theories (Small, 2001). As shown in Figures 7d and 7e, ISW fission occurs in both E2-4 and E2-5. There are, however, significant differences in the results due to difference in energetics. There are four leading waves visible in the small amplitude case (E2-5). For the intermediate amplitude case (E2-3) there are again four waves, but they are larger. For the large amplitude case (E2-4) there are five along with a tail of smaller-amplitude waves. As such, we can conclude that the initial wave amplitude does not appear to be a critical factor for the fission of ISWs on the shelf, but it does impact properties of the generated HIWs.

The effect of stratification on ISW fission is another aspect requiring investigation. For the two-layer model employed in this study, the exact question to answer is how the thickness of the upper layer affects the fission process. Experiments E2-6 and E2-7 are designed to this end. The thickness of the upper layer (h_1) in E2-6 and E2-7 is set as 30 and 50 m, respectively, both of which are substantially smaller than that in E2-3. Note that the minimum water depth is 100 m over Topo 2, meaning that there is no critical region in E2-6 and the critical region in E2-7 is very close to the right boundary of the model domain. As shown in Figure 7f, the depression ISW in E2-6 preserves its waveform during the entire course of propagation from the deep water to the shelf. And in E2-E7, the ISW starts to develop asymmetry in the wave rear after propagating for 5 hr (Figure 7g). Although the results in E2-7 and E2-6 show some differences, no fission occurs in either case. By contrast, in E2-3 fission develops as the ISW passes the critical region, and the ISW eventually fissions into a group of HIWs as it continues shoaling. Therefore, we can conclude that the existence of both the critical region determined by stratification and an extended propagating region is the dynamical cause of ISW fission.

5.2. Application to Observations at Station B

To examine generation process of the HIWs observed at Station B, we now conduct a further experiment E1 using Topo 1. Here the thickness of the upper layer is set as $h_1 = 30$ m according to the measured stratification in Figure 6b. The initial wave amplitude is set as $\eta_0 = -15$ m to represent an ISW of depression. According to the sensitivity experiments using Topo 2, the dissipation term and the shoaling effect term in equation (4) are both omitted here. As indicated in the satellite images shown in Figure 3, there is an underwater bump on the path of ISW to Station B, between $x = 7$ km and $x = 20$ km in Topo 1 as compared to Topo 2. As such, there are two critical regions over Topo 1 as shown in Figure 7h, one near $x = 11$ km and the other near $x = 17$ km. As one would expect, the ISW preserves its waveform before approaching the first critical region. On passing this critical region, the rear of the wave gets steeper and the isopycnal behind the leading depression is raised above its equilibrium depth by $t = 3$ h. During further propagation, the leading wave of depression fades away, but the steep rear of the wave fissions into five waves at $x = 15$ km. The number of the rank-ordered waves increases as the waves pass the second critical region. Sixteen waves have been generated by $t = 7.5$ hr, and more waves are generated as the waves shoal further onshore. The waves continue fissioning after passing the second critical region and propagating in the region with $h_1 < h_2$. Deeper water behind the bump makes the leading waves propagate faster and become more dispersive, resulting in a lengthening of the length of the wave

Table 2
Experimental Parameters for the Numerical Simulations With the Fully Nonlinear Model Based on Continuous Stratification.

Case #	Topography	η_0 (m)	Stratification	K (m^2/s)
Topo1-Stra1-S	Topo 1	-15	Stra1	10^{-5}
Topo1-Stra1	Topo 1	-46	Stra1	10^{-5}
Topo1-Stra1-vis	Topo 1	-46	Stra1	10^{-4}
Topo2-Stra1-vis0	Topo 2	-46	Stra1	0
Topo2-Stra1	Topo 2	-46	Stra1	10^{-5}
Topo2-Stra1-vis	Topo 2	-46	Stra1	10^{-4}
Topo2-Stra1-visL	Topo 2	-46	Stra1	10^{-3}
Topo2-Stra2	Topo 2	-48	Stra2	10^{-5}
Topo2-Stra3	Topo 2	-40	Stra3	10^{-5}
Topo2-Stra4	Topo 2	-40	Stra4	10^{-5}
Topo2-Stra1-S	Topo 2	-15	Stra1	10^{-5}
Topo2-Stra1-L	Topo 2	-76	Stra1	10^{-5}

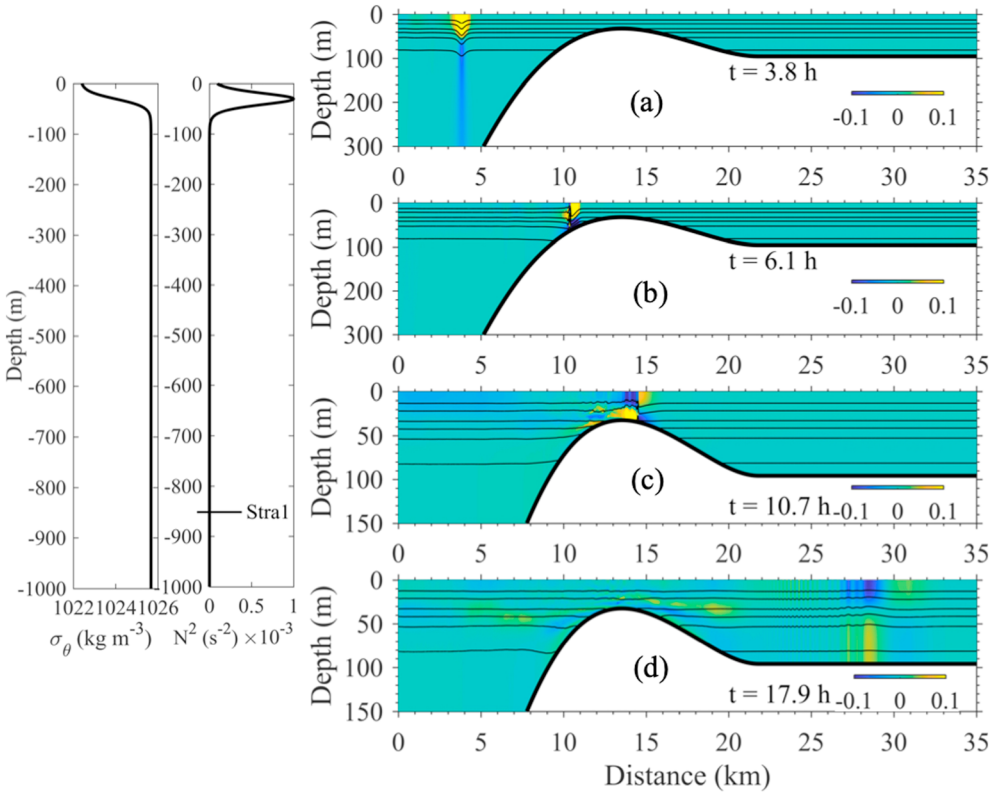

Figure 9. Simulation snapshots of horizontal velocity (color) and density field (contour) at (a) $t = 3.8$ hr, (b) $t = 6.1$ hr, (c) $t = 10.7$ hr, and (d) $t = 17.9$ hr for the case Topo1-Stra1-S. The two left panels indicate the stratification profiles, that is, potential density and buoyancy frequency.

train. As such, an internal wave train consisting of more than 26 waves in a long wave packet with a range of 13 km is generated.

In order to compare with the moored observations in a qualitative way, we transform the results of the simulation to the time series of the interface displacement at a mooring site. This is accomplished by dividing the spatial variation of the interface displacement (i.e., the results shown in Figure 7h) by the propagation speed of the wave packet. The latter can be directly estimated from the simulation. Here two sites located at $x = 2$ km and $x = 32$ km are selected to represent locations where the waves remain in deep water (and thus free of fission) and where Station B is approached, respectively. The propagation speed of wave packet is 1.21 m/s at $x = 2$ km, and 0.83 m/s on reaching $x = 32$ km. As shown in Figure 3, there are two wave packets shoaling towards Station B. The distance between the two wave packets is 12.89 km in Figure 3b, suggesting that they would reach Station B after about 4.3 hr. This time interval is shorter than the tidal period. The second wave packet is possibly formed from the steepening of an inertial-gravity wave as a consequence of radiation damping due to the rotational effects (Helfrich & Grimshaw, 2008). Therefore, we can construct the interface displacement at different locations by combining the satellite observations shown in Figure 3 and the simulation results shown in Figure 7h.

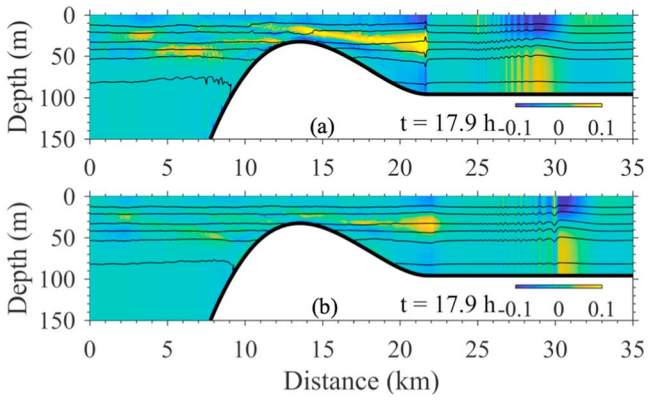

Figure 10. Similar to Figure 9d but for cases (a) Topo1-Stra1 with larger initial wave amplitude and (b) Topo1-Stra1-vis using larger viscosity.

In Figure 8, we show the time series of the interface displacement at $x = 2$ km and at $x = 32$ km, respectively, as a result of the propagation and evolution of two initial ISWs separated by 5 hr. As shown in Figure 8a, the waves remain ISWs of depression at $x = 2$ km. In contrast, however, the waves have evolved into trains of HIWs by the time they approach $x =$

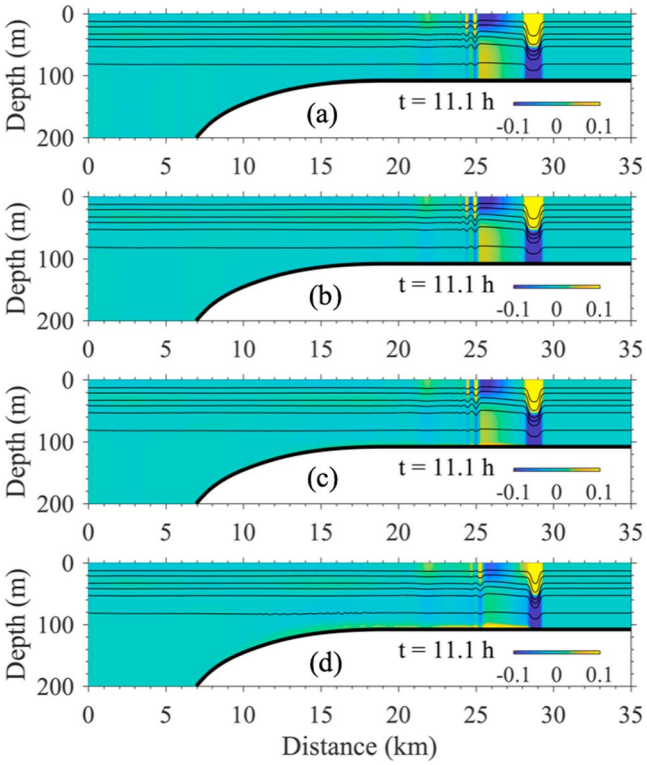

Figure 11. Simulation snapshots of horizontal velocity (color) and density field (contour) at $t = 11.1$ hr for cases (a) Topo2-stra1-vis0, (b) Topo2-stra1, (c) Topo2-stra1-vis, and (d) Topo2-stra1-visL. They differ in the value of viscosity.

32 km due to fissioning (Figure 8b). Clearly, the structures shown in Figure 8b are very close to what we observed at Station B, suggesting that the continuous occurrence of HIWs at Station B can be explained by the fission of shoaling ISWs.

6. Investigation Based on a Fully Nonlinear Model

The above features of ISW fission obtained from the two-layer weakly nonlinear theory are now tested and further investigated using a fully nonlinear nonhydrostatic internal gravity wave model (Lamb, 1994, 2007; Lamb & Warn-Varnas, 2015). The effects of rotation are neglected here given the much shorter shoaling time than the local inertial period. The model is two-dimensional and uses the rigid-lid, Boussinesq, and incompressible approximations. The governing equations are

$$\boldsymbol{u}_t + \boldsymbol{u}\cdot\nabla\boldsymbol{u} = -\frac{1}{\rho_0}\nabla p - \frac{\rho}{\rho_0}g\hat{k} + \nu\nabla^2\boldsymbol{u}, \tag{5}$$

$$\rho_t + \boldsymbol{u}\cdot\nabla\rho = \kappa\nabla^2\rho, \tag{6}$$

$$\nabla\cdot\boldsymbol{u} = 0, \tag{7}$$

where $\boldsymbol{u} = (u,w)$ is the velocity vector. ρ is the density field, ρ_0 is the reference density, p is the pressure field, g is the gravitational acceleration, ν is the kinematic viscosity, and κ is the diffusivity. For simulations with viscosity and diffusion, a form of viscosity/diffusivity of Lamb and Warn-Varnas (2015), coupled with a no-slip bottom boundary condition, is used in this model in the form of $\nu(x,z) = \kappa(x,z) = K$ sech $[(z(x) - H(x)/h_s)]$ so that viscous and diffusion is only large in a lower layer with thickness determined by h_s. Here H is the water depth and $h_s = 10.0$ m is a scale height (Lamb & Warn-Varnas, 2015). The values of K are shown in Table 2. We set up the model with high horizontal resolution of 10 m and 150 vertical grids to resolve shoaling process of ISWs, including wave breaking. All simulations are initialized with an ISW of depression located at $x = -10$ km. The initial ISW is computed by solving for the Dubreil-Jacotin-Long equation (Lamb & Warn-Varnas, 2015), an eigenvalue problem for the isopycnal displacement $\eta(x,z)$ in a channel of finite depth. Detailed configurations of the numerical experiments are provided in Table 2.

We first apply this model to simulate the shoaling ISW with similar conditions as those in the experiment E1 but using a continuous stratification (termed as Topo1-Stra1-S in Figure 9). As shown in Figure 9, the maximum buoyancy frequency is at 30-m depth, indicating that the upper layer $h_1 = 30$ m, and the thickness of the pycnocline is based on the observations in Figure 6b. Snapshots in Figure 9 indicate the evolution of an ISW with an initial wave amplitude of 15 m shoaling over the bathymetry Topo 1: (a) the ISW propagates in the form of a single depression wave before reaching the slope; (b) isopycnals in the front of the wave are almost parallel to the bottom, while the rear of the wave is much steeper. The isopycnal behind the shoaling ISW raises above its equilibrium position and starts to break, when the wave is close to the slope; (c) the wave breaks over the bump in contrast to the experiment E1 in Figure 7h; (d) the breaking wave fissions to a group of small amplitude shorter waves during its further propagation in the shallow water behind the bump.

Based on the experiment Topo1-Stra1-S, in Figure 10 we examine the effects of larger-amplitude wave (Topo1-Stra1) and the influence of larger viscosity (Topo1-Stra1-vis). Increasing the initial wave amplitude from 15 to 46 m visibly results in much larger fission waves (Figure 10a versus 9d). However, the wave amplitude does not increase linearly with the increasing initial wave amplitude due to wave breaking, which results in a mode-2 wave with strong current at $x = 21.6$ km. Moreover, increasing the viscosity (experiment Topo1-Stra1-vis) weakens the mode-2 wave and current near $x = 22$ km (Figures 10a, 10b). Additionally, the wave amplitude and the positive current of the leading wave are strengthened at $x = 30$ km. The wave

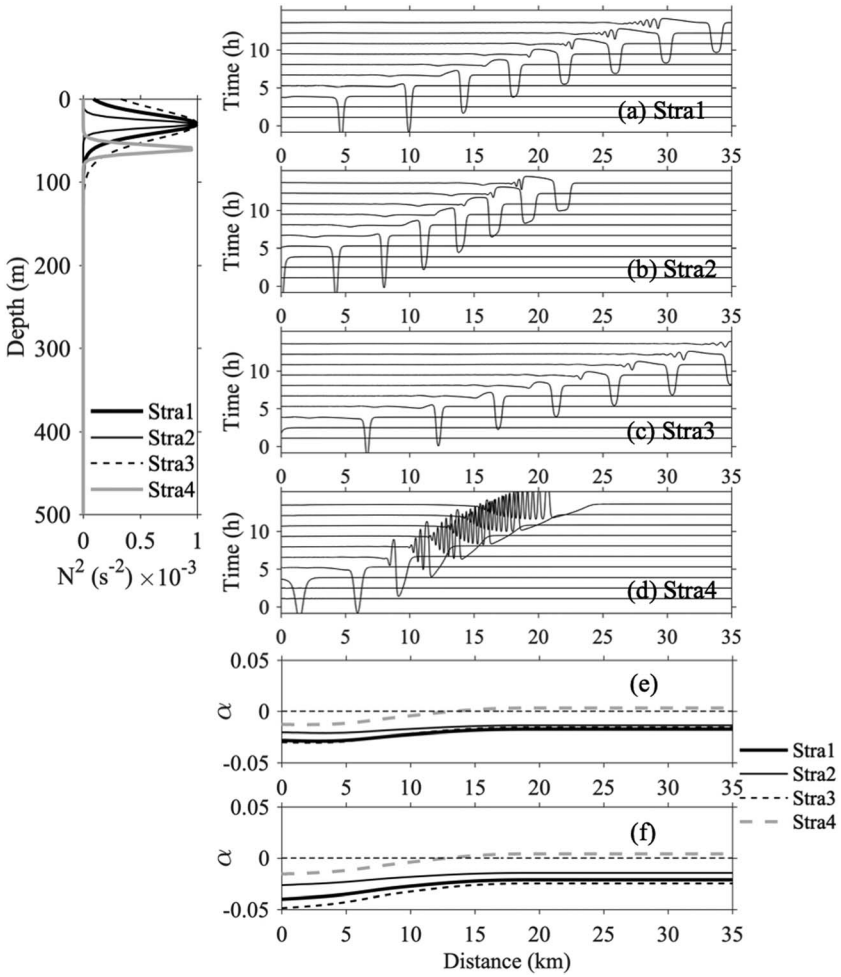

Figure 12. Simulations of cases (a) Topo2-Stra1, (b) Topo2-Stra2, (c) Topo2-Stra3, and (d) Topo2-Stra4, based on corresponding stratification profiles in the left panel. (a-d) The fluctuations of the isopycnal initially at 30-m depth varying with time. Spatial distribution of the quadratic nonlinear coefficient α in the four simulations estimated based on (e) continuous stratification and based on (f) simplified two-layer stratification.

structure is much more visible although the number of the small waves is less than that in Figure 10a due to the viscous effects.

The viscous effects are further investigated using a general bathymetry Topo 2 by removing the underwater bump to reduce the influence of wave breaking. Figure 11 compares results from an inviscid simulation (Topo2-stra1-vis0) with results from simulations with $K = 10^{-5}$ (Topo2-stra1), 10^{-4} (Topo2-stra1-vis) and 10^{-3} m^2/s (Topo2-stra1-visL). In these experiments, the leading ISWs keep their single waveform of depression. During the propagation on the shallow shelf, a group of small amplitude short dispersive waves forms 3 km behind the leading wave. The process is shown in Figure 12a. The noticeable difference among the four simulations is that the length of the leading wave decreases with increasing viscosity, indicating that it has less energy for larger viscosity experiments. For $K = 10^{-3}$ m^2/s, the trailing dispersion is much weaker and the number of waves is less than that in other experiments. However, the value of K is possibly unrealistically large (Lamb & Warn-Varnas, 2015). Lamb and Warn-Varnas (2015) emphasized the significance of viscosity in water depth shallower than 200 m. Our results in Figures 10 and 11 further suggest the significance of viscous effects in modulating waves especially when wave breaking happens in shallow water.

We next consider the sensitivity of ISW fission to variations in stratification, which has been found to play the key role in controlling fission in the two-layer model. Only the sensitivity to the pycnocline depth can

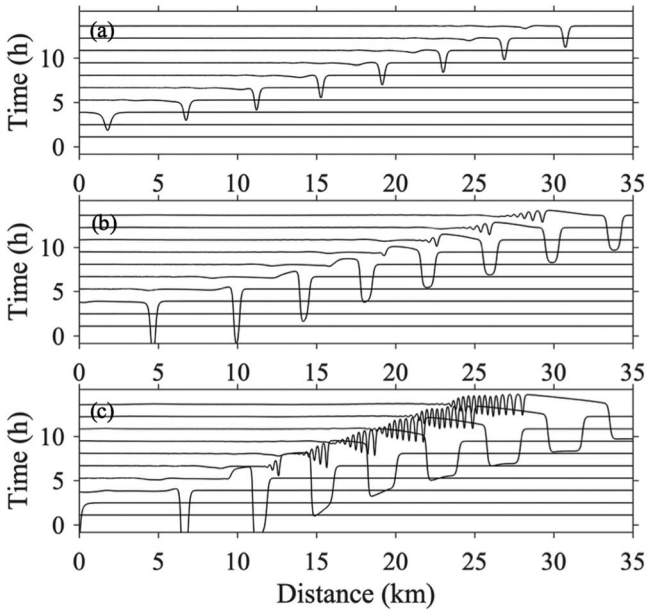

Figure 13. Similar to Figure 12 but for cases (a) Topo2-Stra1-S, (b) Topo2-Stra1, and (c) Topo2-Stra2-L. These cases are different in initial wave amplitude.

be analyzed in a two-layer model. Here we first investigate the effect of the pycnocline thickness, which is illustrated by comparing Topo2-Stra1 with Topo2-Stra2 (thinner pycnocline) and Topo2-Stra3 (thicker pycnocline) in Figures 12a-12c. Their difference indicates that pycnocline thickness affects wave speed and the length of leading wave, as well as the trailing dispersive waves. On the other hand, the effects of the pycnocline depth are also illustrated by comparing Topo2-Stra1 (at 30-m depth) with Topo2-Stra4 (at 60-m depth). A noticeable difference that can be seen in Figure 12d is that the rear of the leading ISW is much steeper at $t = 6.3$ hr for the deeper pycnocline case. Behind the leading wave the isopycnals rise above their equilibrium positions. The raised isopycnals fission into 3 waves at $x = 12.3$ km and subsequently many more waves emerge. In contrast to the fission in Figures 11 and 12a-12c, the ISW of depression in Figure 12d evolves into a group of elevation waves, whose amplitude is much larger and comparable to the initial wave. The result suggests that almost all the ISW energy transfer to the fission waves in experiment Topo2-Stra4. The fission can be predicted using quadratic nonlinear coefficient α. In a continuous stratification, the nonlinear coefficient is defined as $\alpha = \frac{3}{2}\frac{\int_{-H}^{0}(c-U)^2(\partial\phi/\partial z)^3 dz}{\int_{-H}^{0}(c-U)(\partial\phi/\partial z)^2 dz}$, where c is the phase speed of linear long waves, U is the background current, and $\phi(z)$ is the mode-1 eigenfunction. In Figure 12e, estimation of α for the four stratifications indicates that there is only critical region for Stra4, located at $x = 13.4$ km. The calculated critical point is slightly offshore of the fission location in the simulations. For the other three cases, α is negative and fission is weak, α can also be estimated for the equivalent two-layer stratifications by defining the maximum buoyancy frequency layer depth as the pycnocline depth. The results are shown in Figure 12f, which exhibit very similar distributions as their continuous counterparts (Figure 12e). This validates the applicability of a two-layer model in predicting ISW fission. It is thus suggested that ISW fission is not determined by the pycnocline thickness, but by the pycnocline depth. As such, the fission location can be roughly predicted using the critical point.

Although the fission process is well simulated by a two-layer weakly nonlinear model, such a model has deficiencies such as an upper limit in wave amplitude and being invalid in simulating breaking of shoaling ISWs (Lamb & Xiao, 2014). The deficiency of the two-layer weakly nonlinear model in wave amplitude limit can be complemented using a continuous fully nonlinear model. Here we consider the sensitivity of ISW fission to the initial wave amplitude by comparing Topo2-Stra1-S ($\eta_0 = 15$ m), Topo2-Stra1 ($\eta_0 = 46$ m), and Topo2-Stra1-L ($\eta_0 = 76$ m). The length of the leading wave is longer, and the amplitude and number of the trailing waves are greater for larger-amplitude ISWs (Figure 13). This result implies that fission may be an effective path for ISW energy loss, in addition to wave breaking as shown in Figure 10. However, variations of the initial wave amplitude do not change the polarity and dominant role of energy of the leading waves before reaching a critical point.

7. Conclusions and Discussion

In contrast to intensive investigations of ISW generation and propagation, there remain limited studies on the degeneration of ISWs further onshore. To this end, we have investigated the properties and generation mechanism of the HIWs observed on the northeastern shelf of the SCS. The structure of the waves was captured in detail by a moored ADCP. The characteristics of internal waves revealed by the 15-hr measurements suggest that these internal waves were HIWs with periods ranging from 4.3 to 6.8 min. In contrast to the regular occurrence of ISWs, the HIWs were continuously recorded in our moored observations. We hypothesize that the fission of ISWs over shoaling topography is responsible for the generation of the observed HIWs. This hypothesis is supported by satellite observations showing that a single ISW evolves into a wave train as it propagates to our observation site. Fission of ISWs in this study region can also be predicted from a simplified analytical model (Tappert & Zabusky, 1971; Zheng et al., 2001). Our analysis suggested that the study region is favorable for ISW fission. To investigate the mechanism of ISW fission, dynamical analysis was

then conducted using a two-layer weakly nonlinear numerical model based on the RLW equation. Implemented with model parameters characteristic of the study region, the simulation results were qualitatively consistent with the field measurements. As shown in the sensitivity experiments, although the properties of shoaling internal waves were all affected by the dissipation and shoaling terms, and by the initial wave amplitude, none of these conditions was the critical factor for the ISW fission on the shelf. In fact, fission occurs after the polarity conversion of ISWs in the critical region. The existence of both the critical region and an extended propagating region is of definitive importance to ISW fission.

The simulation results of the two-layer weakly nonlinear model have been further compared by applying a fully nonlinear nonhydrostatic internal gravity wave model using continuous stratifications. Sensitivity experiments were carried out to consider the effects of bathymetry, viscosity, stratification and initial wave amplitude. Similar to the conclusion made using the two-layer weakly nonlinear model, the pycnocline depth plays a key role in controlling ISW fission. This result suggests that the critical point can be used to predict the location of ISW fission and polarity conversion. The consistency of the continuously stratified fully nonlinear model and the two-layer weakly nonlinear model simulations validates the applicability of two-layer models. However, different from the two-layer model results, fission starts to occur before ISWs reach the critical point in continuously stratified model simulations. In the sensitivity experiments, the viscosity and diffusion are found to be more significant in shallow water, especially when wave breaking occurs. Other conditions, such as the pycnocline thickness and initial wave amplitude could influence the wave speed, wavelength, and trailing waves, but most wave energy is still retained in the leading ISW before wave breaking. The fission in the trailing waves is much weaker than that results from deeper pycnocline depth. We can see that the fully nonlinear numerical model with continuous stratification has more advantages in simulating the small-amplitude short trailing waves, as well as large-amplitude ISWs, wave breaking and higher-mode waves.

For the ADCP measurements, Scotti et al. (2005) pointed out that the standard conversion algorithm from beam to earth coordinates should be modified when measuring short internal waves using ADCP. In their case, short waves had wavelengths of 100-200 m at a site with water depth of 85 m in the Massachusetts Bay, and the standard conversion algorithm was violated by these short internal waves. Potential errors might be induced by strong sheared currents in coastal oceans (Mirshak & Kelley, 2009; Scotti et al., 2005). In this study, the averaged period of HIWs is 4.3-6.8 min and the phase speed is estimated to be 0.76 m/s, giving a wavelength of about 196.1 to 310.1 m. We did not apply the modified conversion algorithm (Scotti et al., 2005) in this study but would do that when investigating the shorter trailing waves after 7:10 on July 14, 2011 shown in Figure 2.

The present study was motivated by our attempt to understand the generation mechanism of the observed HIWs. Fission of a shoaling ISW is shown to be responsible for generating dispersive HIWs on the shelf. HIWs have been frequently observed in other locations, for example, in the Massachusetts Bay (Scotti et al., 2008) and on the Oregon continental shelf (Moum et al., 2003; Moum & Smyth, 2006). In contrast to the case studied here, in the Massachusetts Bay the generation of HIWs is due to the nonlinear-dispersive evolution of the internal tides (Scotti et al., 2008), which forms an undular bore that subsequently shoals and breaks. Scotti et al. (2008) investigated the shoaling of a wave packet, comparing observations with simulations using a fully nonlinear numerical model and a simple two-layer hydrostatic model. The observations and simulations showed the generation of HIWs (see their Figures 3 and 10) associated with strong breaking events. The shoaling waves in their study did not pass through a critical point where ISWs change polarity. The generation mechanism of the HIWs is fundamentally different from what we have proposed and tested in this study. The continuous appearance of HIWs was also observed on the Oregon continental shelf (Moum & Smyth, 2006), where the wave characteristics were revealed by determining the nonhydrostatic pressure disturbance. In an earlier study in this region, HIWs were proposed to play a key role in causing intensified turbulent dissipation (Moum et al., 2003). In our study region, statistical analysis of the ISW distribution (Bai et al., 2014) suggests that the continental slope of the northeastern SCS is not only a local generation site of ISWs but also a region with intense ISW dissipation. A question naturally arises as to the role the fission process plays in the dissipation of ISWs. This is, however, beyond the scope of the present study, and both observations and dynamical analysis are required to address this question. Moreover, in the ocean the ISWs always coexist with ambient currents (which are sometimes rather strong), including for example the barotropic and baroclinic tidal currents and/or quasi-steady shear currents. The impacts of ambient currents on

fission process of ISWs and the three-dimensional dynamics of ISW fission, such as focusing of shoaling ISWs, remain to be explored.

Acknowledgments
This work was supported by the National Natural Science Foundation of China (41622601, 91858201, 41721005, and U1405233), the National Key R&D Program of China (2016YFC1401404), and the National Basic Research Program of China (2015CB954004). X. Bai was supported by the International Postdoctoral Exchange Fellowship Program (2018) from China Postdoctoral Council, China Scholarship Council (201506310091), and the Postgraduates Exchange Program of the Graduate School of Xiamen University. K. G. Lamb was supported by the Natural Sciences and Engineering Research Council of Canada (NSERC). The MODIS true-color images employed in this study were obtained from NASA's LAADS (Level-1 and Atmosphere Archive and Distribution System) website (http://ladsweb.nascom.nasa.gov/index.html). The bathymetry data were downloaded from ETOPO1 Global Relief Model (http://www.ngdc.noaa.gov/mgg/global/global.html). The simulations were done at the facilities of Shared Hierarchical Academic Research Computing Network (SHARC-NET) and Compute/Calcul Canada. The mooring data used in this study can be requested from the corresponding author (zyliu@xmu.edu.cn).

References

Alford, M. H., Lien, R.-C., Simmons, H., Klymak, J., Ramp, S., Yang, Y. J., et al. (2010). Speed and evolution of nonlinear internal waves transiting the South China Sea. *Journal of Physical Oceanography*, *40*(6), 1338–1355. https://doi.org/10.1175/2010JPO4388.1

Apel, J. R., Badiey, M., Ching-Sang Chiu, Finette, S., Headrick, R., Kemp, J., et al. (1997). An overview of the 1995 SWARM shallow-water internal wave acoustic scattering experiment. *IEEE Journal of Oceanic Engineering*, *22*(3), 465–500. https://doi.org/10.1109/48.611138

Bai, X., Liu, Z., Li, X., Chen, Z., Hu, J., Sun, Z., & Zhu, J. (2013). Observations of high-frequency internal waves in the southern Taiwan Strait. *Journal of Coastal Research*, *29*(6), 1413–1419.

Bai, X., Liu, Z., Li, X., & Hu, J. (2014). Generation sites of internal solitary waves in the southern Taiwan Strait revealed by MODIS true-colour image observations. *International Journal of Remote Sensing*, *35*(11-12), 4086–4098. https://doi.org/10.1080/01431161.2014.916453

Buijsman, M. C., Legg, S., & Klymak, J. (2012). Double-ridge internal tide interference and its effect on dissipation in Luzon Strait. *Journal of Physical Oceanography*, *42*(8), 1337–1356. https://doi.org/10.1175/JPO-D-11-0210.1

Cai, S., Gan, Z., & Long, X. (2002). Some characteristics and evolution of the internal soliton in the northern South China Sea. *Chinese Science Bulletin*, *47*(1), 21–27. https://doi.org/10.1360/02tb9004

Fu, K.-H., Wang, Y.-H., Laurent, L. S., Simmons, H., & Wang, D.-P. (2012). Shoaling of large amplitude nonlinear internal waves at Dongsha Atoll in the northern South China Sea. *Continental Shelf Research*, *37*(1–7), 1–7. https://doi.org/10.1016/j.csr.2012.01.010

Grimshaw, R., Guo, C., Helfrich, K., & Vlasenko, V. (2014). Combined effect of rotation and topography on shoaling oceanic internal solitary waves. *Journal of Physical Oceanography*, *44*(4), 1116–1132. https://doi.org/10.1175/JPO-D-13-0194.1

Grimshaw, R., Pelinovsky, E., Talipova, T., & Kurkina, O. (2010). Internal solitary waves: propagation, deformation and disintegration. *Nonlinear Processes in Geophysics*, *17*(6), 633–649. https://doi.org/10.5194/npg-17-633-2010

Helfrich, K. R., & Grimshaw, R. (2008). Nonlinear disintegration of the internal tide. *Journal of Physical Oceanography*, *38*(3), 686–701. https://doi.org/10.1175/2007JPO3826.1

Jackson, C., Arvelyna, Y., & Asanuma, I. (2011). High-frequency nonlinear internal waves around the Philippines. *Oceanography*, *24*(1), 90–99. https://doi.org/10.5670/oceanog.2011.06

Klymak, J. M., Alford, M. H., Pinkel, R., Lien, R.-C., Yang, Y. J., & Tang, T.-Y. (2011). The breaking and scattering of the internal tide on a continental slope. *Journal of Physical Oceanography*, *41*(5), 926–945. https://doi.org/10.1175/2010JPO4500.1

Klymak, J. M., Pinkel, R., Liu, C.-T., Liu, A. K., & David, L. (2006). Prototypical solitons in the South China Sea. *Geophysical Research Letters*, *33*, L11607. https://doi.org/10.1029/2006GL025932

Lamb, K. G. (1994). Numerical experiments of internal wave generation by strong tidal flow across a finite amplitude bank edge. *Journal of Geophysical Research*, *99*(C1), 843–864. https://doi.org/10.1029/93JC02514

Lamb, K. G. (2007). Energy and pseudoenergy flux in the internal wave field generated by tidal flow over topography. *Continental Shelf Research*, *27*(9), 1208–1232. https://doi.org/10.1016/j.csr.2007.01.020

Lamb, K. G. (2014). Internal wave breaking and dissipation mechanisms on the continental slope/shelf. *Annual Review of Fluid Mechanics*, *46*(1), 231–254. https://doi.org/10.1146/annurev-fluid-011212-140701

Lamb, K. G., & Warn-Varnas, A. (2015). Two-dimensional numerical simulations of shoaling internal solitary waves at the ASIAEX site in the South China Sea. *Nonlinear Processes in Geophysics*, *22*(3), 289–312. https://doi.org/10.5194/npg-22-289-2015

Lamb, K. G., & Xiao, W. (2014). Internal solitary waves shoaling onto a shelf: Comparisons of weakly-nonlinear and fully nonlinear models for hyperbolic-tangent stratifications. *Ocean Modelling*, *78*, 17–34. https://doi.org/10.1016/j.ocemod.2014.02.005

Lien, R.-C., D'Asaro, E. A., Henyey, F., Chang, M.-H., Tang, T.-Y., & Yang, Y.-J. (2012). Trapped core formation within a shoaling nonlinear internal wave. *Journal of Physical Oceanography*, *42*(4), 511–525. https://doi.org/10.1175/2011JPO4578.1

Liu, A. K., Chang, Y. S., Hsu, M. K., & Liang, N. K. (1998). Evolution of nonlinear internal waves in the East and South China Seas. *Journal of Geophysical Research*, *103*(C4), 7995–8008. https://doi.org/10.1029/97JC01918

Mirshak, R., & Kelley, D. E. (2009). Inferring propagation direction of nonlinear internal waves in a velocity sheared background flow. *Journal of Atmospheric and Oceanic Technology*, *26*(3), 615–625. https://doi.org/10.1175/2008JTECHO632.1

Moum, J. N., Farmer, D. M., Smyth, W. D., Armi, L., & Vagle, S. (2003). Structure and generation of turbulence at interfaces strained by internal solitary waves propagating shoreward over the continental shelf. *Journal of Physical Oceanography*, *33*(10), 2093–2112. https://doi.org/10.1175/1520-0485(2003)033<2093:SAGOTA>2.0.CO;2

Moum, J. N., & Smyth, W. D. (2006). The pressure disturbance of a nonlinear internal wave train. *Journal of Fluid Mechanics*, *558*, 153–177. https://doi.org/10.1017/S0022112006000036

Orlanski, I. (1976). A simple boundary condition for unbounded hyperbolic flows. *Journal of Computational Physics*, *21*(3), 251–269. https://doi.org/10.1016/0021-9991(76)90023-1

Orr, M. H., & Mignerey, P. C. (2003). Nonlinear internal waves in the South China Sea: Observation of the conversion of depression internal waves to elevation internal waves. *Journal of Geophysical Research*, *108*(C3), 3064. https://doi.org/10.1029/2001JC001163

Ramp, S. R., Tang, T. Y., Duda, T. F., Lynch, J. F., Liu, A. K., Chiu, C. S., et al. (2004). Internal solitons in the northeastern South China Sea. Part I: Sources and deep water propagation. *IEEE Journal of Oceanic Engineering*, *29*(4), 1157–1181. https://doi.org/10.1109/JOE.2004.840839

Scotti, A., Beardsley, R. C., Butman, B., & Pineda, J. (2008). Shoaling of nonlinear internal waves in Massachusetts Bay. *Journal of Geophysical Research*, *113*, C08031. https://doi.org/10.1029/2008JC004726

Scotti, A., Butman, B., Beardsley, R. C., Alexander, P. S., & Anderson, S. (2005). A modified beam-to-earth transformation to measure short-wavelength internal waves with an Acoustic Doppler Current Profiler. *Journal of Atmospheric and Oceanic Technology*, *22*(5), 583–591. https://doi.org/10.1175/JTECH1731.1

Shroyer, E. L., Moum, J. N., & Nash, J. D. (2009). Observations of polarity reversal in shoaling nonlinear internal waves. *Journal of Physical Oceanography*, *39*(3), 691–701. https://doi.org/10.1175/2008JPO3953.1

Small, J. (2001). A nonlinear model of the shoaling and refraction of interfacial solitary waves in the ocean. part I: Development of the model and investigations of the shoaling effect. *Journal of Physical Oceanography*, *31*(11), 3163–3183. https://doi.org/10.1175/1520-0485(2001)031<3163:ANMOTS>2.0.CO;2

Tappert, F., & Zabusky, N. (1971). Gradient-induced fission of solitons. *Physical Review Letters*, *27*(26), 1774–1776. https://doi.org/10.1103/PhysRevLett.27.1774

Vlasenko, V., Stashchuk, C. G., & Chen, X. (2010). Multimodal structure of baroclinic tides in the South China Sea. *Nonlinear Processes in Geophysics*, *17*(5), 529–543. https://doi.org/10.5194/npg-17-529-2010

Zhao, Z., Klemas, V. V., Zheng, Q., & Yan, X.-H. (2003). Satellite observation of internal solitary waves converting polarity. *Geophysical Research Letters*, *30*(19), 1988. https://doi.org/10.1029/2003GL018286

Zhao, Z., Klemas, V. V., Zheng, Q., & Yan, X.-H. (2004). Remote sensing evidence for baroclinic tide origin of internal solitary waves in the northeastern South China Sea. *Geophysical Research Letters*, *31*, L06302. https://doi.org/10.1029/2003GL019077

Zheng, Q., Klemas, V. V., Yan, X.-H., & Pan, J. (2001). Nonlinear evolution of ocean internal solitons propagating along an inhomogeneous thermocline. *Journal of Geophysical Research*, *106*(C7), 14,083–14,094. https://doi.org/10.1029/2000JC000386

Zheng, Q., Susanto, R. D., Ho, C.-R., Song, Y. T., & Xu, Q. (2007). Statistical and dynamical analyses of generation mechanisms of solitary internal waves in the northern South China Sea. *Journal of Geophysical Research*, *112*, C03021. https://doi.org/10.1029/2006JC003551